Monthly Notices
of the
ROYAL ASTRONOMICAL SOCIETY

MNRAS **491,** 4116–4130 (2020)
Advance Access publication 2019 November 20

doi:10.1093/mnras/stz3240

The evolution of galaxy intrinsic alignments in the MassiveBlackII universe

Aklant K. Bhowmick ,★ Yingzhang Chen, Ananth Tenneti , Tiziana Di Matteo and Rachel Mandelbaum

McWilliams Center for Cosmology, Department of Physics, Carnegie Mellon University, Pittsburgh, PA 15213, USA

Accepted 2019 November 17. Received 2019 November 11; in original form 2019 May 1

ABSTRACT

We investigate the redshift evolution of the intrinsic alignments (IAs) of galaxies in the MassiveBlackII (MBII) simulation. We select galaxy samples above fixed subhalo mass cuts ($M_h > 10^{11,12,13}\,\mathrm{M}_\odot\,h^{-1}$) at $z = 0.6$ and trace their progenitors to $z = 3$ along their merger trees. Dark matter components of $z = 0.6$ galaxies are more spherical than their progenitors while stellar matter components tend to be less spherical than their progenitors. The distribution of the galaxy–subhalo misalignment angle peaks at ∼10 deg with a mild increase with time. The evolution of the ellipticity–direction (ED) correlation amplitude $\omega(r)$ of galaxies (which quantifies the tendency of galaxies to preferentially point towards surrounding matter overdensities) is governed by the evolution in the alignment of underlying dark matter (DM) subhaloes to the matter density of field, as well as the alignment between galaxies and their DM subhaloes. At scales ~ 1 Mpc h^{-1}, the alignment between DM subhaloes and matter overdensity gets suppressed with time, whereas the alignment between galaxies and DM subhaloes is enhanced. These competing tendencies lead to a complex redshift evolution of $\omega(r)$ for galaxies at ~ 1 Mpc h^{-1}. At scales > 1 Mpc h^{-1}, alignment between DM subhaloes and matter overdensity does not evolve significantly; the evolution of the galaxy–subhalo misalignment therefore leads to an increase in $\omega(r)$ for galaxies by a factor of ∼4 from $z = 3$ to 0.6 at scales > 1 Mpc h^{-1}. The balance between competing physical effects is scale dependent, leading to different conclusions at much smaller scales (~ 0.1 Mpc h^{-1}).

Key words: gravitational lensing: weak – hydrodynamics – methods: numerical – galaxies: formation.

1 INTRODUCTION

The shapes and orientations of galaxies have an intrinsic correlation with respect to those of nearby galaxies and the overall matter distribution; this effect is known as galaxy intrinsic alignments (IAs; see Joachimi et al. 2015; Kiessling et al. 2015; Kirk et al. 2015, and references therein for review; Troxel & Ishak 2015). The importance of IA is two-fold: (i) IA emerges as a natural outcome of the current paradigm of galaxy formation in the Λ cold dark matter cosmological model, as emphasized also in state-of-the-art cosmological hydrodynamic simulations that include direct modelling of galaxy formation (e.g. Tenneti et al. 2014; Chisari et al. 2015; Velliscig et al. 2015; Hilbert et al. 2017). IA is therefore a promising probe for galaxy formation physics. (ii) If not properly modelled and removed, IA is a significant source of systematic bias in inferring cosmological parameters in weak lensing studies (Krause, Eifler & Blazek 2016). Many of the upcoming surveys like the Large Synoptic Survey Telescope (LSST; Ivezić et al. 2008; Abell et al. 2009;), Euclid (Laureijs et al. 2011), and the Wide-Field Infrared Survey Telescope (WFIRST; Spergel et al. 2015) aim to determine the dark energy equation of state to very high precision using weak lensing, and IA is one of the major sources of astrophysical systematic uncertainty for such studies (Mandelbaum 2018). The existence of IA in galaxies with correlations out to 100 h^{-1} Mpc scales has been firmly established in observational data (e.g. Mandelbaum et al. 2006; Hirata et al. 2007; Joachimi et al. 2011; Singh, Mandelbaum & More 2015). An understanding of IAs and their scaling with galaxy mass and redshift is therefore crucial to mitigating this effect in weak lensing studies, and is also a good diagnostic for galaxy formation physics.

Intrinsic alignments have been studied using analytical methods such as the linear model (Catelan, Kamionkowski & Blandford 2001), the non-linear alignment model (Bridle & King 2007), and the full tidal alignment model (Blazek, Vlah & Seljak 2015). While these methods are easy to implement, also requiring few computational resources, they inevitably rely on assumptions about the alignment of galaxies and the underlying tidal field. This

★ E-mail: akbhowmi@andrew.cmu.edu

limitation can be overcome by state-of-the-art cosmological hydrodynamic simulations (e.g. Dubois et al. 2014; Vogelsberger et al. 2014; Khandai et al. 2015; Schaye et al. 2015), which can directly probe the impact of galaxy formation physics on the shapes and alignments of galaxies and the relation to their dark matter counterparts (haloes/subhaloes) and the tidal fields themselves. Therefore, in recent years galaxy shapes and alignments have been extensively studied using hydrodynamic simulations (e.g. Chisari et al. 2015; Tenneti, Mandelbaum & Di Matteo 2016; Chisari et al. 2017; Hilbert et al. 2017).

An important step towards understanding galaxy intrinsic alignments is to study their redshift evolution. This has been initiated by a series of works (Tenneti et al. 2015a) using the MassiveBlackII (MBII) hydrodynamic simulation (Khandai et al. 2015), including a detailed study of the redshift evolution of galaxy shapes, alignment with respect to host halo/subhalo, and associated shape–density correlation functions. A noteworthy feature of these works was that the sampling of galaxies was based on fixed subhalo mass cut ($\gtrsim 10^{11}$, 10^{12}, 10^{13} $\mathrm{M}_{\odot}\,h^{-1}$) at each redshift (from $z \sim 0.06$ to 1); this is somewhat representative of cuts in observed galaxy samples in properties such as stellar mass or magnitude, which are known to correlate with the host subhalo mass. However, with such an approach, the resulting redshift evolution may be dominated by the effects of sample selection. In order to study the *intrinsic* redshift evolution (i.e. separated from the effects of sample selection), we must select samples of galaxies at a given redshift and trace their progenitors to higher redshifts.

In this work, we study the redshift evolution of IA properties of MBII galaxies by making subhalo mass cuts at a single fixed redshift ($z \sim 0.6$) and then tracing the properties of their progenitors along a merger tree. In Section 2, we outline the basic methodology and definitions. In Section 3, we study the redshift evolution of galaxy properties (axis ratios, galaxy−subhalo misalignment angle, and density–shape correlation functions) on the merger tree. We summarize our key results in Section 4.

2 METHODS

2.1 MBII simulation

We briefly describe MBII, which is a state-of-the-art cosmological hydrodynamic simulation of structure formation (Khandai et al. 2015). MBII is evolved from $z = 159$ to $z = 0.06$ in a cubic periodic box of comoving volume $V_{\rm box} = (100\,h^{-1}\mathrm{Mpc})^3$ and a gravitational smoothing length of $\epsilon = 1.85\,h^{-1}$ kpc. The box contains 2×1792^3 particles (dark matter+gas). The mass of a single dark matter particle and a single gas particle is $m_{\rm DM} = 1.1 \times 10^7\,h^{-1}\,\mathrm{M}_{\odot}$ and $m_{\rm gas} = 2.2 \times 10^6\,h^{-1}\,\mathrm{M}_{\odot}$, respectively. The cosmological parameters used in the simulation are based on WMAP7 (Komatsu et al. 2011) with amplitude of matter fluctuations $\sigma_8 = 0.816$, spectral index $n_{\rm s} = 0.96$, mass density parameter $\Omega_{\rm m} = 0.275$, cosmological constant density parameter $\Omega_{\Lambda} = 0.725$, baryon density parameter $\Omega_{\rm b} = 0.046$, and Hubble parameter $h = 0.702$. Halos are identified using a friends-of-friends (FOF) halo finder (Davis et al. 1985) with a linking length of 0.2 times the mean particle separation.

2.2 Galaxy identification

Here, we describe how galaxies are identified in MBII. Galaxies are defined to be the stellar component of *subhaloes*, which are locally overdense, self-bound particle groups within a larger parent group (FOF halo). The subhalo catalogues are generated using the substructure finder SUBFIND on the halo catalogues. In SUBFIND, for each particle in the parent group, a local density is estimated using the positions of a prescribed number of nearest neighbours. After identifying the local peaks in density field, it rebuilds the parent group by adding particles in the order of decreasing density. In doing so, a saddle point is eventually reached that connects two disjoint overdense regions. The smaller structure is then identified as a candidate substructure. For further implementation details, see the original paper (Springel et al. 2001).

2.3 Constructing the galaxy merger tree

In this section, we describe the key steps involved in the construction of the galaxy merger tree. The machinery to obtain the merger trees involved post-processing the simulation outputs using ROCKSTAR (Behroozi, Wechsler & Wu 2012a) halo/subhalo finder along with CONSISTENT-TREES (Behroozi et al. 2012b). However, these codes can only be run on dark matter particles. In order to obtain the galaxy merger trees, we first identify galaxies using SUBFIND. We then finally map the SUBFIND galaxies to the dark matter subhaloes identified within ROCKSTAR-CONSISTENT TREES. In the process, both ROCKSTAR and SUBFIND catalogues had to be used to construct the galaxy merger tree.

To begin with, halo/subhalo merger trees were identified by running the ROCKSTAR (Behroozi et al. 2012a) halo/subhalo finder along with CONSISTENT-TREES (Behroozi et al. 2012b), both of which are described in the following two subsections.

2.3.1 *ROCKSTAR*

ROCKSTAR (or 'Robust Overdensity Calculation using K-Space Topologically Adaptive Refinement') is an algorithm based on adaptive hierarchical refinement of FOF groups. Primary FOF groups are first identified using an FOF finder. Within each FOF group, a hierarchy of FOF subgroups (in phase space) is identified using an adaptive refinement of the linking length. The FOF subgroups at the lowest (deepest) level of the hierarchy are then converted into seed haloes. Starting with the lowest level of the hierarchy, the FOF subgroup particles are assigned to the seed haloes based on phase space distances; this process is repeated for the higher levels of the hierarchy until all particles of the parent FOF group have been assigned to the halo. After assigning all the particles, the host–subhalo relationship is calculated by assigning a seed halo to be a *subhalo* of the closest seed halo (within the same FOF group) with larger number of assigned particles. This process is performed until all the seed haloes are either *host haloes* or *subhaloes*. For further implementation details, see the original paper (Behroozi et al. 2012a).

2.3.2 *CONSISTENT-TREES*

We build a merger tree for our ROCKSTAR haloes/subhaloes using CONSISTENT-TREES algorithm (Behroozi et al. 2012b). CONSISTENT-TREES is an extension to traditional *particle-based* (constructed by tracing trajectories of halo/subhalo particles across different time-steps) tree building algorithms that can potentially compromise the *continuity* of halo/subhalo properties across simulation time-steps, due to the issues listed in section 2.2 of Behroozi et al. (2012b).

CONSISTENT-TREES resolves the foregoing problem by tracing (in addition to particles) a subset of halo/subhalo properties that include halo mass, maximum circular velocity, halo position, and bulk velocity. A major component of the algorithm is to ensure continuity in these halo properties by construction. This is achieved by running a particle-based tree finder and establishing preliminary links between progenitor haloes (at time-step t_{n-1}) and descendant haloes (at time-step t_n). The subsequent steps consist of the following actions:

(i) Gravitationally tracing the positions of descendant haloes from t_n to t_{n-1} to obtain their most likely progenitors at t_{n-1}; removing progenitors whose properties do not resemble the most likely progenitors of the corresponding descendants.

(ii) For each descendant halo at t_n that lacks a progenitor at t_{n-1} after step (i), a *phantom* progenitor is assigned with halo properties identical to its most likely progenitor at t_{n-1}; however, those descendant haloes that do not have progenitors for a sufficiently large sequence of time-steps are removed.

(iii) Finally, if a halo at t_{n-1} has no descendant at t_n after step (ii), it is *merged* with a halo (at t_n) in its vicinity that has the strongest tidal field; additionally, the halo is removed as a statistical fluctuation if it is too far away from other haloes to experience any significant tidal field.

(iv) Steps (i) to (iii) are iterated over the range of time-steps (where each iteration corresponds a pair of time slices t_{n-1} and t_n) from final time t_f to initial time t_i. This establishes a lineage of haloes over the time range t_i to t_f.

Readers who are interested in more details are encouraged to refer to section 5 of Behroozi et al. (2012b).

2.3.3 *Constructing galaxy merger tree: matching ROCKSTAR and SUBFIND*

The subhalo merger trees obtained using ROCKSTAR-CONSISTENT TREES are dark matter only. In order to construct the galaxy merger tree for our SUBFIND galaxies, we must match the subhaloes on the ROCKSTAR merger tree to our SUBFIND galaxies. We perform the following steps for the matching:

(i) For a given ROCKSTAR subhalo (mass $M_h^{\rm RS}$) denoted by SUBHALO-RS, we select all SUBFIND subhaloes (with mass $M_h^{\rm sub}$) that satisfy $0.5 \times M_h^{\rm RS} < M_h^{\rm sub} < 2 \times M_h^{\rm RS}$ and within a maximum distance of $5 \times R_{\rm vir}^{\rm RS}$, where $R_{\rm vir}^{\rm RS}$ is the virial radius of the ROCKSTAR subhalo. We then choose the SUBFIND subhalo that is closest to the ROCKSTAR subhalo, denoted by SUBHALO-RS-SUB.

(ii) For the SUBFIND subhalo SUBHALO-RS-SUB, we select all ROCKSTAR subhaloes (with mass $M_h^{\rm sub}$) that satisfy $0.5 \times M_h^{\rm sub} < M_h^{\rm RS} < 2 \times M_h^{\rm sub}$ and within a maximum distance of $5 \times R_{\rm vir}^{\rm sub}$, where $R_{\rm vir}^{\rm sub}$ is the virial radius of the SUBFIND subhalo. We then choose the ROCKSTAR subhalo that is closest to the SUBFIND subhalo, denoted by SUBHALO-RS-SUB-RS.

(iii) If (and only if) we retrieve the original ROCKSTAR subhalo at the end of step (ii), i.e. SUBHALO-RS-SUB-RS is identical to SUBHALO-RS, we say that SUBHALO-RS (from the ROCKSTAR merger tree) and SUBHALO-RS-SUB (from the SUBFIND catalogue) have been *matched*.

In order to generate a corresponding SUBFIND galaxy merger tree from a ROCKSTAR merger tree, every ROCKSTAR subhalo on the tree must be matched with a SUBFIND galaxy for the redshift range of our interest ($z_i \le z \le z_f$). If the matching fails at any redshift within ($z_i \le z \le z_f$), the entire tree is discarded. We quantify the matching success rate by defining a *matching efficiency* $\eta_{\rm matching}$ as the ratio of the number of matched SUBFIND trees over the number of original ROCKSTAR trees (present before matching). Fig. 1 shows $\eta_{\rm matching}$ as a function of M_h at various values of z_f ($z_i = 0.6$). For $z_f = 1.5$ (red line), the efficiency is 86 per cent for all masses. At higher z_f, we lose more trees (as expected) and the efficiency decreases to 75–82 per cent for $z_f = 3$. This translates to a total of 27 942 SUBFIND galaxy merger trees with progenitors up to redshift 3. This sample is sufficient for a statistical analysis, and to avoid further decrease in efficiency, we choose not to trace progenitors beyond redshift 3, hereafter defining the redshift range of our study to be $0.6 \le z \le 3$. We chose $z \ge 0.6$ since it is the time period when galaxy formation and merger processes are most active.

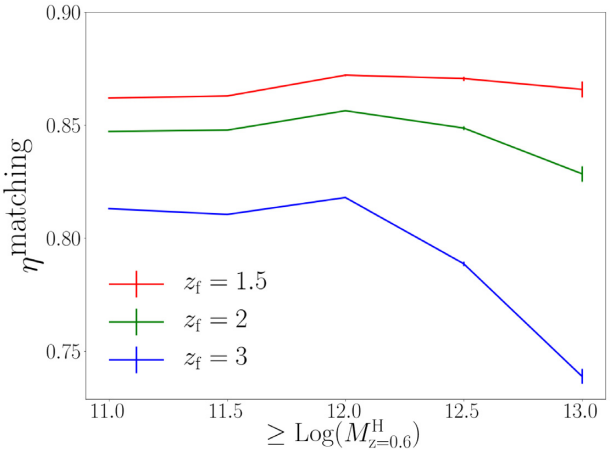

Figure 1. $\eta_{\rm matching}$ is the *matching efficiency*, i.e. the ratio between the number of SUBFIND trees with respect to the original number of ROCKSTAR trees (before matching ROCKSTAR and SUBFIND trees). $1 - \eta_{\rm matching}$ therefore is the fraction of ROCKSTAR trees lost because we could not find a corresponding SUBFIND tree to match with. '$\geq \log(M^H_{z=0.6})$' is the threshold subhalo mass of galaxies selected at $z = 0.6$; z_f is the maximum redshift up to which their progenitors are traced (starting from $z_i = 0.6$).

2.4 Shapes of galaxies and dark matter haloes

We now describe how galaxy shapes are quantified. We model the shapes of the dark matter and stellar matter components of subhaloes as ellipsoids in three dimensions by using the eigenvalues and eigenvectors of the inertia tensor (Bailin & Steinmetz 2005; Tenneti et al. 2014) given by

$$I_{ij} = \frac{\Sigma_n m_n x_{ni} x_{nj} W(r_n)}{\Sigma_n m_n} \quad (1)$$

where m_n is the mass of the $n^{\rm th}$ particle and x_{ni} and x_{nj} represent the i and j component of the position of the $n^{\rm th}$ particle ($0 \le i, j \le 2$). r_n is the distance of the $n^{\rm th}$ particle from the subhalo centre and is given by $r_n^2 = \sum x_{ni}^2$. $W(r_n)$ is a weight function. Several weight functions have been used in the literature. $W(r_n) = 1$ corresponds to an *unweighted* inertia tensor that assigns equal contributions to all stars within the subhalo. However, observationally it is difficult to detect stars in the outskirts of the galaxy; in order to minimize the influence of these regions, one can use

$$W(r_n) = \frac{1}{r_n^2} \quad (2)$$

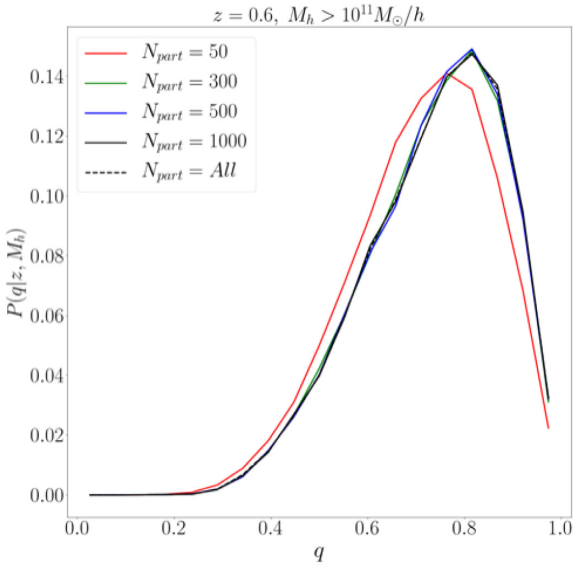

Figure 2. Shape convergence test: normalized histograms of $q = \frac{b}{a}$ of the dark matter component of SAMPLE-TREE galaxies at $z = 0.6$. We show the comparison between shapes determined using all particles in the subhalo with those obtained using a random subsample of $N_{\rm part} = 50, 100, 300, 1000$ particles in the subhalo.

which naturally puts a higher weight on stars closer to the galaxy centre. This corresponds to the *reduced inertia tensor*.

We denote the principal axis directions or eigenvectors (unit vectors) of I_{ij} to be $(\hat{e}_a, \hat{e}_b, \hat{e}_c)$ with corresponding eigenvalues $(\lambda_a, \lambda_b, \lambda_c)$. The lengths of the principal axes (a, b, c) are given by $(\sqrt{\lambda_a}, \sqrt{\lambda_b}, \sqrt{\lambda_c})$. The ellipticities can then be measured by the axis ratios

$$q = \frac{b}{a}, s = \frac{c}{a} \tag{3}$$

where a is the length of the primary (largest) axis. A perfectly spherical subhalo corresponds to $q = s = 1$ and a triaxial halo corresponds to $q \neq s < 1$.

To minimize any possible bias in the measured shape, we adopt an iterative approach wherein we first determine the principal axes and axis ratios using all the particles in the subhalo, thereby determining the ellipsoidal volume. For each successive iteration, we then recalculate the inertia tensor and axis ratios ignoring particles outside the ellipsoidal volume. We repeat this until each iteration leads to $\lesssim 1$ per cent change in a, b and c. In this work, we have used the reduced inertia tensor, along with the iterative scheme, for computing both stellar matter and dark matter shapes, unless stated otherwise.

2.4.1 *Shape convergence test*

We require a sufficiently large number of particles to reliably measure galaxy (subhalo) shapes. Here, we determine the minimum number of particles. Fig. 2 shows the distribution of q (denoted by $P(q|M_h)$) for $z = 0.6$ and $M_h > 10^{11}$ M$_\odot\, h^{-1}$ galaxies. We show $P(q|M_h)$ for different numbers ($N_{\rm part}$) of subsampled dark matter particles within each subhalo. We find that the distributions converge for $N_{\rm part} = 300, 500, 1000$ whereas for $N_{\rm part} = 50$, q is significantly underestimated. Therefore, we assume $N_{\rm part} \geq 300$ in this work to ensure shape convergence; similarly, this choice is also sufficient for the convergence of s. This sets a minimum subhalo mass of our Galaxies to $M_h \sim 3 \times 10^9$ M$_\odot\, h^{-1}$, which limits the subhalo mass and redshift range over which we can construct merger trees. We find that for galaxies with $M_h > 10^{11}$ M$_\odot\, h^{-1}$ at $z = 0.6$, their progenitors have $M_h \gtrsim 3 \times 10^9$ M$_\odot\, h^{-1}$ up to $z = 3$. Therefore, our final choice for the subhalo mass range and redshift range in this work are $M_h > 10^{11}$ M$_\odot\, h^{-1}$ and $0.6 < z < 3$.

2.5 Misalignment angle

To quantify the misalignment between the galaxy (stellar matter component) and its host dark matter subhalo, we calculate the principal axes corresponding to the dark matter and star particles, i.e. $(\hat{e}_a^{\rm DM}, \hat{e}_b^{\rm DM}, \hat{e}_c^{\rm DM})$ and $(\hat{e}_a^*, \hat{e}_b^*, \hat{e}_c^*)$, respectively. The misalignment angle is then defined as the angle between the eigenvectors corresponding to the primary (longest) axes.

$$\theta_{\rm m} = \arccos\left(\left|\hat{e}_a^{\rm DM} \cdot \hat{e}_a^*\right|\right) \tag{4}$$

2.6 Correlation function

The ellipticity–direction (ED) correlation function (Lee et al. 2008) cross-correlates the orientation of the major axis of a subhalo with respect to the large-scale density field. For a subhalo centred at position x with major axis direction $\hat{e}_a$, the ED cross-correlation function is given by

$$\omega(r) = \left\langle |\hat{e}_a(\vec{x}) \cdot \hat{r}(\vec{x} + \vec{r})|^2 \right\rangle - \frac{1}{3} \tag{5}$$

where $\hat{r} = \frac{\vec{r}}{r}$ and $\vec{r}$ is the position vector originating from the subhalo position ($\vec{x}$) to a tracer (galaxy positions or dark matter particle positions) of the large-scale matter distribution around the halo. In this work, we have used the dark matter particle positions as tracers of the matter density field.

3 RESULTS

3.1 Stellar mass–subhalo mass relation

Fig. 3 shows the subhalo total (dark matter+gas+stars+black hole) mass (M_h) versus stellar mass (M_*) relation of SAMPLE-TREE galaxies at $z = 0.6$, 1.5, and 3.0 with $M_h > 10^{11}$M$_\odot\, h^{-1}$ at $z = 0.6$. As expected, M_h and M_* are strongly correlated and both decrease with increasing redshift. The leftmost panel presents the full sample (by definition of SAMPLE-TREE) of galaxies above $M_h > 10^{11}$ M$_\odot\, h^{-1}$. It is instructive to compare these predictions to those of semi-empirical models. The prediction from the semi-empirical model of Behroozi et al. (2013) is shown as a dashed black line; they assume a parametric model for the stellar mass versus halo mass relation, and determine the best-fitting parameters of that relation using the observational constraints on the stellar mass function and star formation histories. Note that the semi-empirical models make predictions for central galaxies only, so we compare their prediction to the mean trend of only the central galaxies within SAMPLE-TREE shown as a solid black line. We see that the semi-empirical model predictions are broadly consistent with MBII for $10^{11.5} \lesssim M_h \lesssim 10^{13}$ M$_\odot\, h^{-1}$. At $M_h \gtrsim 10^{13}$ M$_\odot\, h^{-1}$ and $M_h \lesssim 10^{11.5}$ M$_\odot\, h^{-1}$, the semi-empirical model predicts somewhat lower stellar masses compared to MBII.

The middle and rightmost panels of Fig. 3 correspond to the progenitors of the $z = 0.6$ galaxies from the leftmost panel. As redshift increases along the merger tree, the M_h–M_* relation does not significantly change either in slope or intercept, broadly consistent

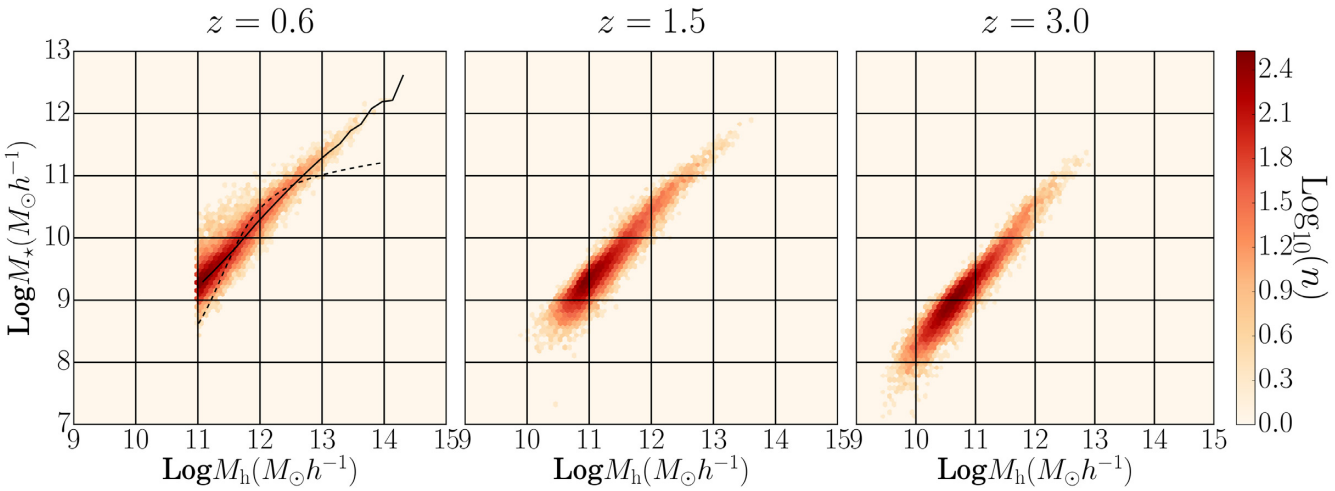

Figure 3. The 2D histograms show the dark matter mass (M_h) versus stellar mass (M_*) relation of galaxies (and dark matter subhaloes) on 27 942 trees corresponding to $M_h > 10^{11}\mathrm{M}_\odot\, h^{-1}$ galaxies at $z = 0.6$ (leftmost panel) and their main progenitors at $z = 1.5$ (middle panel) and $z = 3$ (rightmost panel). Additionally, in the leftmost panel the solid black line corresponds to the mean relations for the central galaxies at $z = 0.6$; we compare this to the dashed black line, which corresponds to the mean relations for the central galaxies predicted using the semi-empirical model of Behroozi, Wechsler & Conroy (2013).

with predictions from semi-analytical models (Mitchell et al. 2016) as well as observations (Leauthaud et al. 2012). This implies that galaxies grow in stellar mass and dark matter mass at roughly the same rate as they evolve along the merger tree.

As the subhalo mass strongly correlates with stellar mass, and therefore also correlates with other observable properties such as luminosity, star formation rate, we shall hereafter use subhalo mass cuts to construct the various galaxy samples defined in the next section for the rest of this work.

3.2 List of galaxy samples: definitions and notations

Before we discuss the rest of the results, we describe the types of galaxy samples that we consider in this work.

(i) SAMPLE-TREE: The primary sample of interest consists of galaxies on the merger tree. We select galaxies with different subhhalo mass cuts (M_h) at $z = 0.6$ and trace their progenitors to $z = 3$ using the methods described in Sections 2.3. Hereafter, we shall refer to this sample as SAMPLE-TREE. For example, the sample name '$\mathtt{SAMPLE\text{-}TREE}$: $M_h > 10^{11}$ $\mathrm{M}_\odot\, h^{-1}$: $z = 2$' refers to galaxies at $z = 2$ that are progenitors of the $M_h > 10^{11}$ $\mathrm{M}_\odot\, h^{-1}$ galaxies as selected at $z = 0.6$. Using this sample, we study the redshift evolution of IA properties of galaxies, without having to consider the impact of evolution due to sample selection.

(ii) SAMPLE-MCUT: The secondary sample of interest is obtained using the selection criterion of Tenneti et al. (2015a). Here, we select galaxy samples with a fixed subhalo mass cut applied at all redshifts. Hereafter, we shall refer to this sample as SAMPLE-MCUT. For example, the sample name '$\mathtt{SAMPLE\text{-}MCUT}$: $M_h > 10^{11}$ $\mathrm{M}_\odot\, h^{-1}$: $z = 2$' refers to all galaxies at $z = 2$ with $M_h > 10^{11}$ $\mathrm{M}_\odot\, h^{-1}$. With this sample, the observed redshift evolution of IA properties is a combination of *intrinsic* redshift evolution effects, and the evolution due to sample selection.

(iii) SAMPLE-RANDOM: To interpret the impact of requiring galaxies to be a part of a merger tree, it will be necessary to look at differences in IA properties between a progenitor (merger tree) galaxy and a randomly chosen galaxy of similar mass. To do this, we construct a galaxy sample by randomly drawing galaxies from the full sample at some redshift (all galaxies in the simulation snapshot), such that the total (dark matter+gas+stars+black hole) mass function is modulated to be identical to that of SAMPLE-TREE (progenitor) galaxies at the same redshift. We shall refer to this as sample SAMPLE-RANDOM. For example, the sample name '$\mathtt{SAMPLE\text{-}RANDOM}$: $M_h > 10^{11}$ $\mathrm{M}_\odot\, h^{-1}$: $z = 2$' refers to a random sample of galaxies at $z = 2$ whose mass function is identical (by construction) to '$\mathtt{SAMPLE\text{-}TREE}$: $M_h > 10^{11}$ $\mathrm{M}_\odot\, h^{-1}$: $z = 2$'.

3.3 Evolution of galaxy shapes and misalignment angles

In this subsection, we will investigate how the shapes of galaxies (and dark matter subhaloes), described by axis ratios $q = \frac{b}{a}$ and $s = \frac{c}{a}$, and the misalignments between stellar and dark matter components evolve with redshift along the merger tree. Fig. 4 shows an illustration of the evolution of a single simulated galaxy along the merger tree from $z = 3$ to $z = 0.6$. We can see that the shape of the dark matter component (yellow ellipse) becomes more spherical with decreasing redshift. Furthermore, at $z = 3$, the stellar matter is significantly misaligned with respect to the dark matter, but the alignment becomes stronger as redshift decreases. In the following subsections, we shall show that the foregoing trends persist for the overall distribution of shapes and misalignment angles for the entire set of SAMPLE-TREE galaxies.

3.3.1 Shape

Fig. 5 shows the distributions $P(q|z, M_h)$ and $P(s|z, M_h)$ of axis ratios q and s, respectively. In Section 2.4.1, we established that $\gtrsim$300 particles are required to reliably measure the shape; this dictates our choice of minimum subhalo mass threshold of $M_h > 10^{11}$ $\mathrm{M}_\odot\, h^{-1}$ at $z = 0.6$. The solid and dashed lines correspond to SAMPLE-TREE and SAMPLE-MCUT, respectively. The bottom panels show the ratio between the axis ratio distributions of SAMPLE-TREE and SAMPLE-MCUT galaxies.

Subhalo mass dependence on the merger tree: We first focus on shapes of dark matter subhaloes. For SAMPLE-TREE galaxies (solid lines), we see that as subhalo mass increases, $P(q|z, M_h)$ and $P(s|z, M_h)$ (for dark matter) are increasingly skewed towards

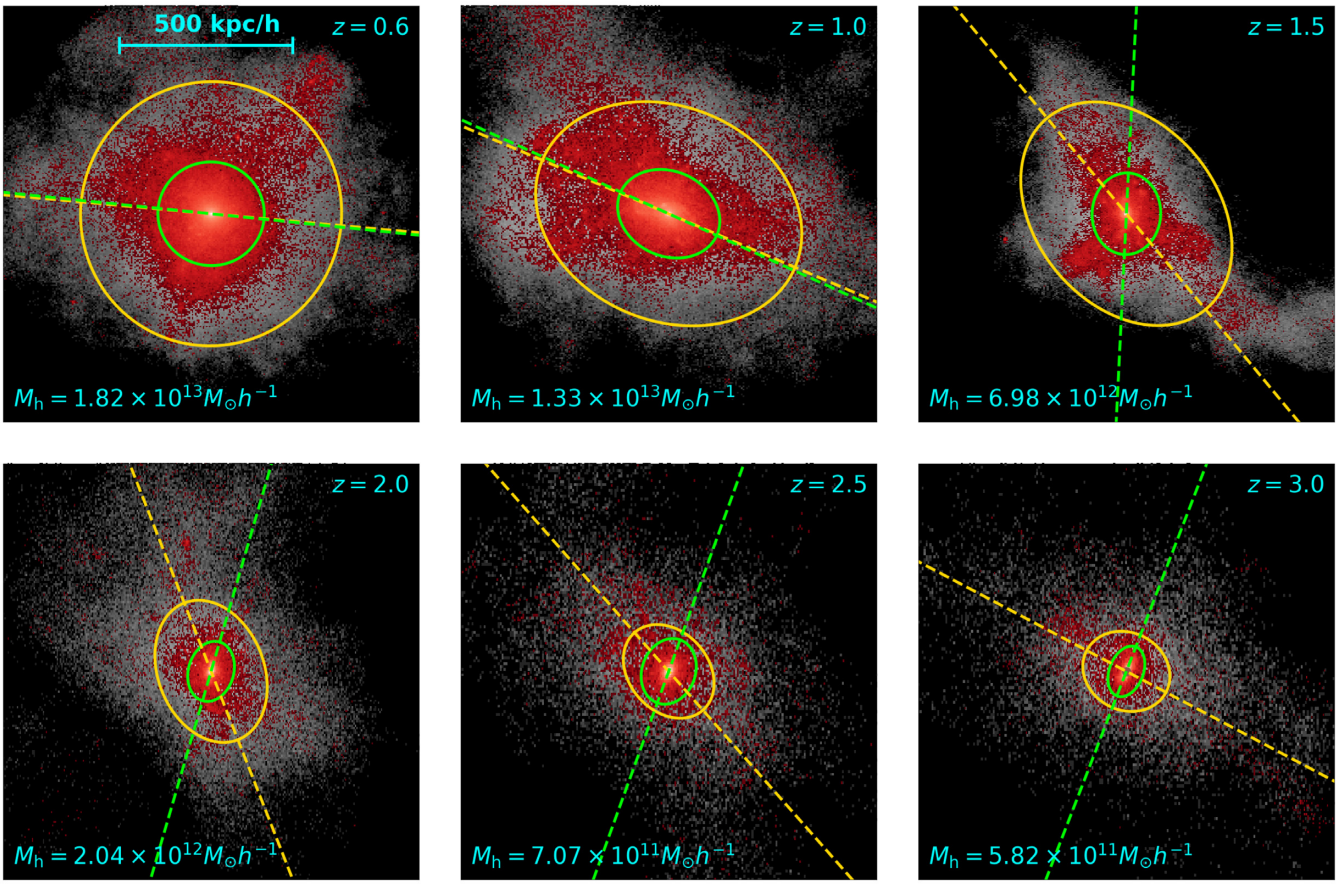

Figure 4. A 2D illustrative example of the evolution of an MBII galaxy on the merger tree. The red histograms show the distribution of stars and grey histograms show the distribution of underlying dark matter. The yellow ellipse represents the shape identified using dark matter particles, while the green ellipse represents the shape identified using stellar matter particles; the yellow and green dashed lines are their corresponding major axis directions. We can see that the subhalo shape is becoming more spherical from $z = 3$ to $z = 0.6$. Furthermore, the alignment between stellar matter and dark matter shapes is becoming stronger as we go from $z = 3$ to $z = 0.6$.

lower values of q and s. This is more clearly seen in the mean values of q and s in Fig. A1. This implies that as subhalo mass increases, galaxies on the merger tree become less spherical at fixed redshift. This is also true for SAMPLE-MCUT galaxies (dashed lines) and has been well established in previous studies (Hopkins, Bahcall & Bode 2005; Allgood et al. 2006; Tenneti et al. 2015a); therefore, it is not surprising that it persists for galaxies on the merger tree.

For the shapes of the stellar matter component, the dependence on subhalo mass at $z \lesssim 1.5$ is the same as that of the dark matter component for both $P(q|M_h)$ and $P(s|M_h)$, also seen in Tenneti et al. (2015a). In other words, at $z \lesssim 1.5$ more massive galaxies have less spherical shapes for the stellar matter component (the mass dependence is seen much more clearly in Fig. A2). However, this result does not persist all the way up to $z \sim 3$. In fact, we see that the mass dependence of $P(q|M_h)$ is reversed (i.e. $P(q|M_h)$ skews towards higher values with increasing subhalo mass) at $z \sim 3$ while $P(s|M_h)$ has no significant mass dependence at $z \sim 3$. Therefore, we find that at $z \sim 3$, the sphericity of the stellar matter component of galaxies increases with increasing subhalo mass.

To summarize the above trends, we find that

(i) the shapes of the dark matter components of galaxies become less spherical with increasing subhalo mass;

(ii) for the stellar matter components, the shapes become less spherical with increasing subhalo mass at $z \lesssim 1.5$. The trend starts to reverse at $z \gtrsim 1.5$ and by $z \sim 3$, the shapes become more spherical with increasing subhalo mass.

Redshift evolution on the merger tree: We first focus on the shapes of dark matter subhaloes. For SAMPLE-TREE galaxies (solid lines), we see that for all three panels, as redshift decreases, the peaks of $P(q|z, M_h)$ and $P(s|z, M_h)$ (for dark matter) shift towards higher values of q and s. This implies that as redshift decreases, galaxies on the merger tree evolve to become more spherical. This is also true for SAMPLE-MCUT galaxies (dashed lines), as was previously reported in Tenneti et al. (2015a). It is also noteworthy that our results are consistent with Hopkins et al. (2005), which investigated the evolution of shapes of cluster-sized haloes ($M_h > 2 \times 10^{13}$ M$_\odot$ h^{-1}) in N-body simulations over roughly the same range of redshifts.

The shape evolution of the stellar matter component has significant differences compared to that of dark matter (as already hinted in the discussion on the subhalo mass dependence). For instance, $P(s|z, M_h)$ tends towards being less spherical as redshift decreases. This trend is opposite to that of dark matter. However, note also that the overall evolution of $P(s|z, M_h)$ is significantly weaker for stellar matter than for dark matter. For $P(q|z, M_h)$, the evolution is more complicated and depends on the subhalo mass threshold. For $M_h > 10^{11}$ M$_\odot$ h^{-1}, there is no significant evolution. On the other hand, for $M_h > 10^{12}$ M$_\odot$ h^{-1} and $M_h > 10^{13}$ M$_\odot$ h^{-1}, the evolution

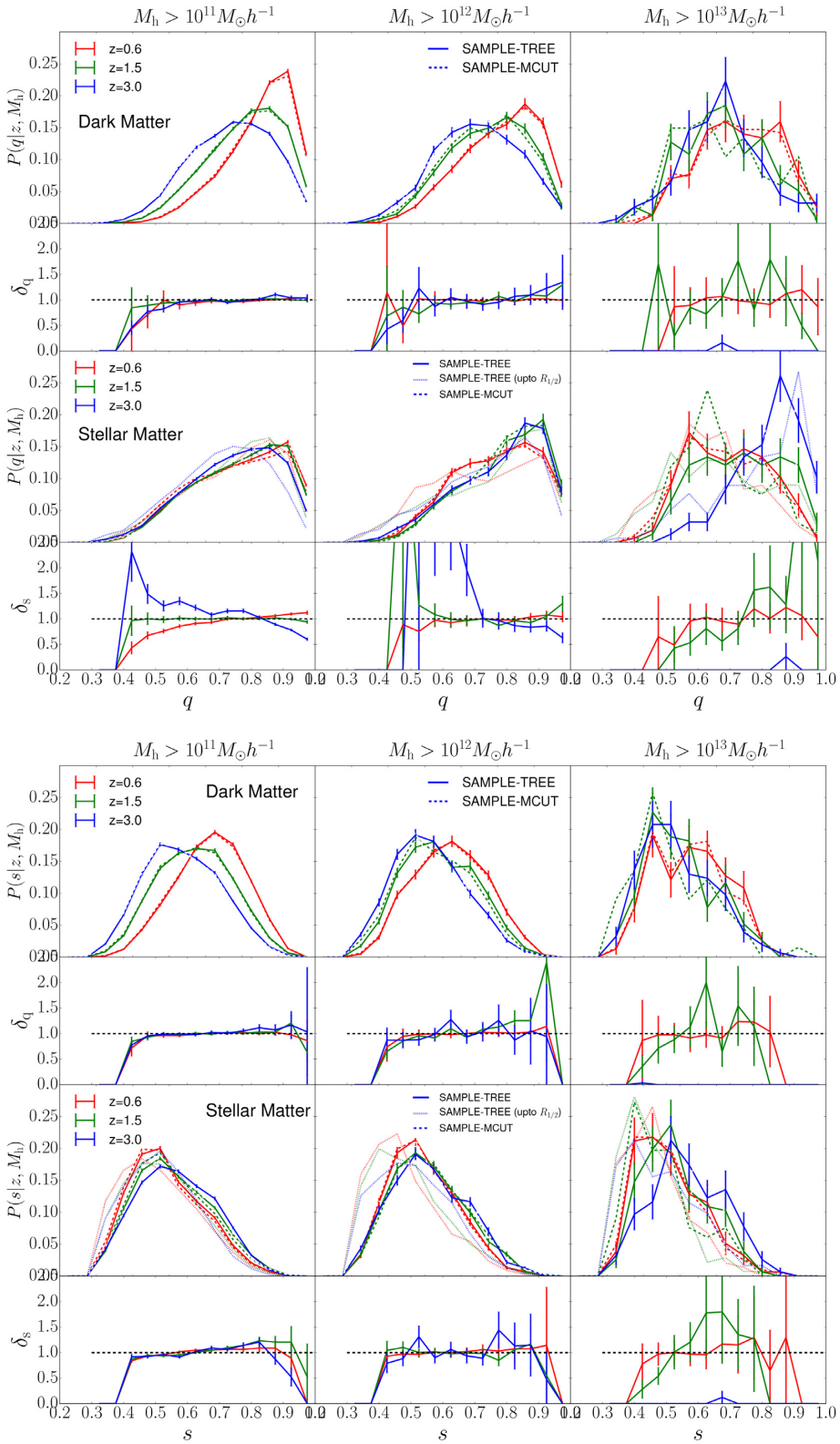

Figure 5. Distribution of 3D galaxy shapes: $P(q|z, M_h)$ (top) and $P(s|z, M_h)$ (bottom) show the normalized probability distributions of axis ratios $q = \frac{b}{a}$ and $s = \frac{c}{a}$ of dark/stellar matter components of galaxies (subhaloes). Solid lines and dashed lines correspond to galaxy samples `SAMPLE-TREE` and `SAMPLE-MCUT`, respectively (see Section 3.2 for definition of galaxy samples). δ_q and δ_s correspond to the ratio of $P(q|z, M_h)$ and $P(s|z, M_h)$, respectively, between `SAMPLE-TREE` and `SAMPLE-MCUT` galaxies. The error bars are 1σ Poisson errors. Additionally, in the panels showing stellar shapes, the faded dotted lines show the distributions for stars located within the half-mass radii of the galaxies.

is significant: $P(q|z, M_h)$ is less spherical at $z = 0.6$ compared with $z = 3$.

To summarize the above trends, we find that:

(i) The shapes of the dark matter components of galaxies tend to become more spherical with time.

(ii) The shapes of the stellar matter components of galaxies tend to become less spherical with time, especially for higher mass thresholds.

Comparison with unweighted stellar shapes within the galaxy half-mass radius: As mentioned in Section 2.4, we use the *reduced* (iterative) inertia tensor so as to minimize the effect of stars in the outer regions of galaxies. However, it is instructive to see whether our overall results (shape evolution) change if the stellar shapes are computed using stars strictly within the galaxy half-mass radius $R_{1/2}$ (with all the stars given the same weight). It is important to note that if we simply use the *unweighted* (iterative) inertia tensor with an exclusion of all the stars outside a sphere with half-mass radius ($r_n > R_{1/2}$) at every iteration, this would artificially introduce spherical symmetry (Tenneti et al. 2015a), and potentially bias the inferred shapes towards being more spherical. In order to avoid this bias, we instead needed to iteratively converge to an ellipsoidal shape aligned with the respective galaxy, with a volume equal to that of a sphere enclosed by the half-mass radius. The details of the computation have been described in Appendix B. The faded dotted lines in Fig. 5 show the shapes of stellar distributions of SAMPLE-TREE galaxies within the half-mass radii; overall, we find that they are less spherical than that of the solid lines. But most importantly, the redshift evolution of the stellar shapes within the half-mass radius (faded dotted lines) is the same as that of the overall stellar shapes (solid lines) obtained using the *reduced* inertia tensor, i.e. for both prescriptions, the shapes become less spherical with decreasing redshift.

Comparing SAMPLE-TREE and SAMPLE-MCUT : We now compare the axis ratio distributions between SAMPLE-TREE and SAMPLE-MCUT (see ratio plots in Fig. 5).

For the dark matter shapes, we find that the axis ratio distributions of SAMPLE-TREE and SAMPLE-MCUT are broadly consistent, i.e. there is no statistically significant difference in their shapes given the error bars. The fact that this is persistent all the way up to $z = 3$ is noteworthy because at $z = 3$, SAMPLE-MCUT galaxies are significantly more massive than SAMPLE-TREE galaxies. This suggests that at fixed redshift, the subhalo mass is not the sole parameter that determines the shapes of dark matter component of galaxies. In particular, galaxies that are progenitors of lower redshift galaxies above some mass threshold may be less spherical compared to a randomly chosen set of galaxies of similar subhalo mass. In order to show this explicitly, in Fig. 6 we compare the axis ratio distributions (at $z = 3$) of the dark matter components of SAMPLE-TREE galaxies with that of a random sample (SAMPLE-RANDOM) whose mass functions are modulated to be identical to that of SAMPLE-TREE. We see that the axis ratios for SAMPLE-TREE galaxies are smaller than that of SAMPLE-RANDOM galaxies. This is also true in general for $z \gtrsim 1.5$. This solidifies the impression that early galaxies that are progenitors of present-day massive galaxies ($M_h > 10^{11}$ M$_\odot\, h^{-1}$ at $z = 0.6$) are more elliptical (on an average) than a randomly selected galaxy at similar subhalo mass and redshift.

For the stellar matter shapes, the ratio plots show that at $z = 3$, $P(q|M_h)$ for samples with mass thresholds of $M_h > 10^{11}$ M$_\odot\, h^{-1}$ and $M_g > 10^{12}$ M$_\odot\, h^{-1}$ are less spherical for SAMPLE-TREE galaxies compared with SAMPLE-MCUT galaxies. This is because

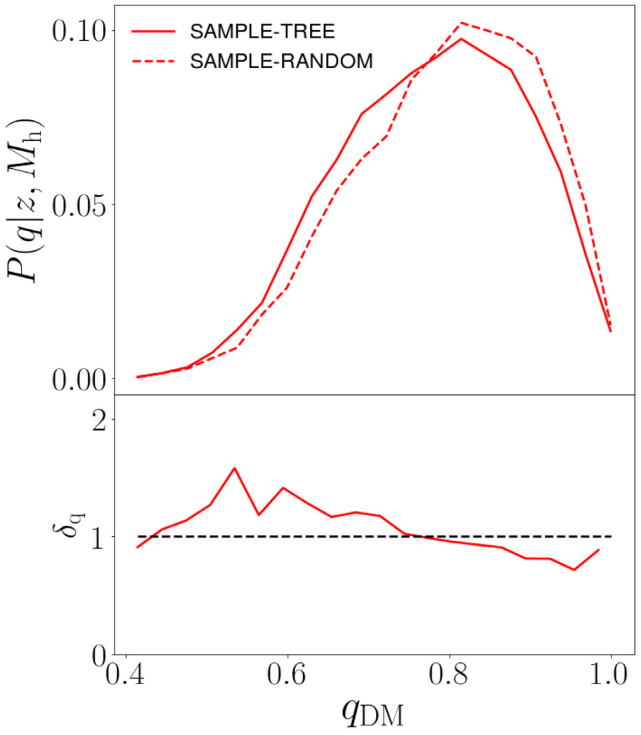

Figure 6. Comparison of the shapes of *progenitor* galaxies and *randomly selected* galaxies of similar mass at $z = z_f = 3$. The solid and dashed lines show $P(q|z, M_h)$ (dark matter component) for SAMPLE-TREE: $M_h > 10^{11}$ M$_\odot\, h^{-1}$: $z = 3$ and SAMPLE-RANDOM: $M_h > 10^{11}$ M$_\odot\, h^{-1}$: $z = 3$ (see Section 3.2 for the sample definitions). δ_q is the ratio between the solid and dashed lines. SAMPLE-RANDOM is constructed to have a mass function identical to that of SAMPLE-TREE progenitors.

SAMPLE-MCUT galaxies are more massive compared to SAMPLE-TREE galaxies at $z = 3$ (we have already shown that stellar matter shapes are more spherical at higher subhalo masses at $z = 3$). $P(s|M_h)$ however has no significant difference between SAMPLE-TREE and SAMPLE-MCUT at $z = 3$ despite the difference in subhalo masses. This is simply because there is insignificant mass dependence in $P(s/M_h)$ for stellar matter at $z = 3$.

The comparison of shapes between SAMPLE-TREE and SAMPLE-MCUT galaxies at $z = 3$ can now be summarized as follows:

(i) For the dark matter components, no difference is found between the shapes of SAMPLE-TREE and SAMPLE-MCUT galaxies at $z = 3$ despite the difference in masses. This is because at $z = 3$ galaxies that are progenitors of $z \sim 0.6$: $M_h \gtrsim 10^{11}$ M$_\odot\, h^{-1}$ galaxies are significantly less spherical (on an average) than a *randomly selected* galaxy of similar subhalo mass and redshift.

(ii) For the stellar matter component, SAMPLE-TREE galaxies are less spherical compared to SAMPLE-MCUT galaxies at $z = 3$. This is because SAMPLE-MCUT galaxies are more massive (which we show to be more spherical for stellar matter component) than SAMPLE-TREE galaxies at $z = 3$.

Shapes of projected distributions: It is instructive to also investigate the evolution of the 2D projected shapes. In Fig. 7, we project the SAMPLE-TREE galaxies on the *xy* plane. As a result, there are only two eigenvectors ($\vec{e}_a$ and $\vec{e}_b$) and eigenvalues (a and b). We compute the distributions of the axis ratios in Fig. 7. We see that the dark matter 2D shapes tend to become more spherical

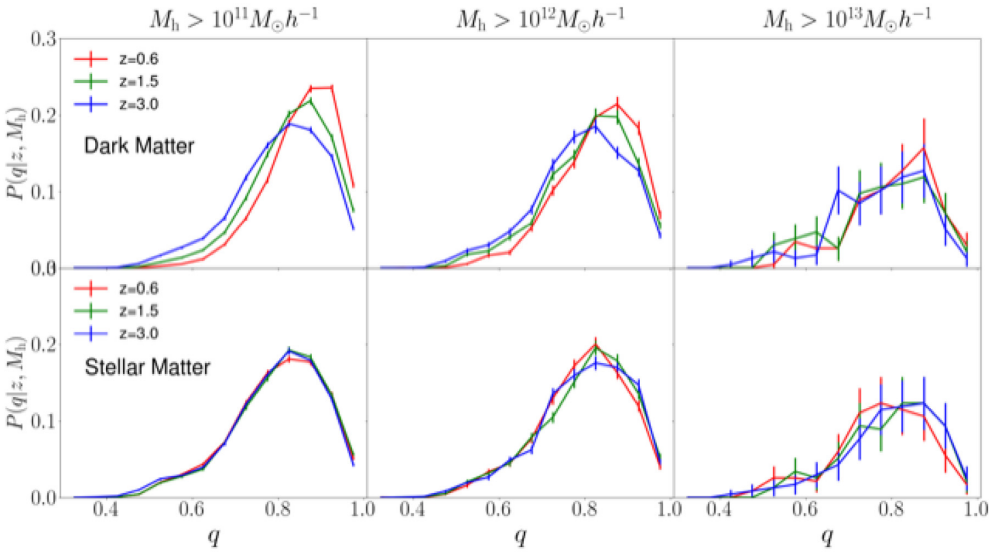

Figure 7. Distribution of projected galaxy shapes: $P(q|z, M_h)$ shows the normalized probability distributions of axis ratio $q = \frac{b}{a}$ obtained by projecting the SAMPLE-TREE galaxies on the *xy* plane. Top and bottom panels correspond to 2D shapes of dark matter and stellar matter, respectively. The error bars are 1σ Poisson errors.

with decreasing redshift, as also seen for 3D shapes. On the other hand, the evolution of the stellar matter 2D shape is significantly smaller compared to dark matter, with no significant evolution for $M_h > 10^{11,12}$ $M_\odot\, h^{-1}$. For $M_h > 10^{13}$ $M_\odot\, h^{-1}$, the 2D shape is slightly less spherical at $z = 0.6$, compared to $z = 3$.

3.3.2 *Misalignment angle*

In this section, we investigate how the misalignment angle of galaxies on the tree evolves with redshift.

The solid lines in Fig. 8 (top panels) show the distribution $P(\theta|z, M_h)$ of misalignment angles (θ) at different redshifts and subhalo mass cuts for SAMPLE-TREE galaxies. The distributions are skewed with a maximum at $\theta_m \sim 5-10$ deg accompanied by a long tail at $\theta_m > 10$ deg, and a sharp fall-off at $\theta_m < 5$ deg. At fixed redshift, as the subhalo mass increases, $P(\theta|M_h)$ skews towards smaller values of θ (seen more clearly in Fig. A3). This implies that more massive galaxies are more aligned with their subhaloes. $P(\theta|M_h)$ skews towards smaller θ as redshift decreases, implying that galaxies evolve over time to become increasingly aligned with their subhaloes, although the evolution is mild.

The evolution of the misalignment angle can be put in the context of existing IA models. The fact that the evolution is mild suggests that it may possibly be mediated by the evolution of the instantaneous tidal field. This is hinted by the fact that the contribution of the instantaneous tidal field is small (compared to observations), as predicted by the analytical model presented in Camelio & Lombardi (2015). In such a scenario, the redshift evolution, contributed by the instantaneous tidal field, can be thought of as a perturbation to the pre-existing alignment ($\theta_m \sim$ 10 deg). Given its strength, the pre-existing alignment is likely set by the primordial (at the formation epoch of these galaxies) tidal field, as assumed in linear alignment models (Catelan et al. 2001; Hirata & Seljak 2004).

We also compare $P(\theta|z, M_h)$ for SAMPLE-TREE galaxies to the predictions for SAMPLE-MCUT galaxies (solid versus dashed lines in Fig. 8 top panels); Fig. 8 (bottom panels) shows the ratio δ_θ. For $M_H > 10^{11,12}$ $M_\odot\, h^{-1}$, we find that $\delta_\theta < 1$ for $\theta < 25$ deg and $\delta_\theta > 1$ for $\theta > 25$ deg at all redshifts. This implies that SAMPLE-TREE galaxies are less aligned with their subhaloes compared to SAMPLE-MCUT galaxies. At $z = 1.5$ and $z = 3$, one would expect this to be the case as SAMPLE-MCUT galaxies are more massive, and therefore more aligned than SAMPLE-TREE galaxies. However, we also see the same effect at $z = 0.6$, where both SAMPLE-MCUT and SAMPLE-TREE galaxies have the same subhalo mass thresholds. This implies that galaxies that formed between $0.6 \lesssim z \lesssim 3$ (i.e. those that do not have progenitors up to $z = 3$) are more aligned with their subhaloes than those that formed at $z > 3$.

Comparison with misalignments of stellar mass within the galaxy half-mass radius: We now investigate how our results for the misalignment angle distributions are affected if we only consider star particles within the galaxy half-mass radius. In Fig. 9, the faded dotted lines show misalignment angle distributions of SAMPLE-TREE galaxies using the unweighted inertia tensor of star particles within the galaxy half-mass radius $R_{1/2}$. We compare them to the solid lines (same as Fig. 8), which were made using the reduced inertia tensor of all star particles in a galaxy (subhalo). For $M_h > 10^{11,12}$ $M_\odot\, h^{-1}$ galaxies (leftmost and middle panels), we see that at $z = 0.6$ (red lines) the faded dotted lines are slightly more aligned compared to the solid lines; the differences tend to decrease at $z = 3$. For $M_h > 10^{13}$ $M_\odot\, h^{-1}$, the error bars are too large for the distributions to be distinguishable (rightmost panel). Most importantly, we find that the overall redshift evolution is the same regardless of the inertia tensor that is used, i.e. galaxies tend to become more aligned with decreasing redshift.

Misalignments in projected distributions: Fig. 10 shows the evolution of the projected galaxy–subhalo misalignment angle (θ_{proj}) distribution from $z = 0.6$ to $z = 3$ for SAMPLE-TREE galaxies. We note that the peak misalignment in projected space is significantly smaller compared to 3D space. This is expected due to the fact that $\theta_{proj} < \theta$ for any given galaxy. Overall, we see that the redshift evolution reported for 3D misalignments can also be seen in the projected space, i.e. the projected stellar distributions of galaxies become more aligned with respect to their dark matter distributions with decreasing redshifts.

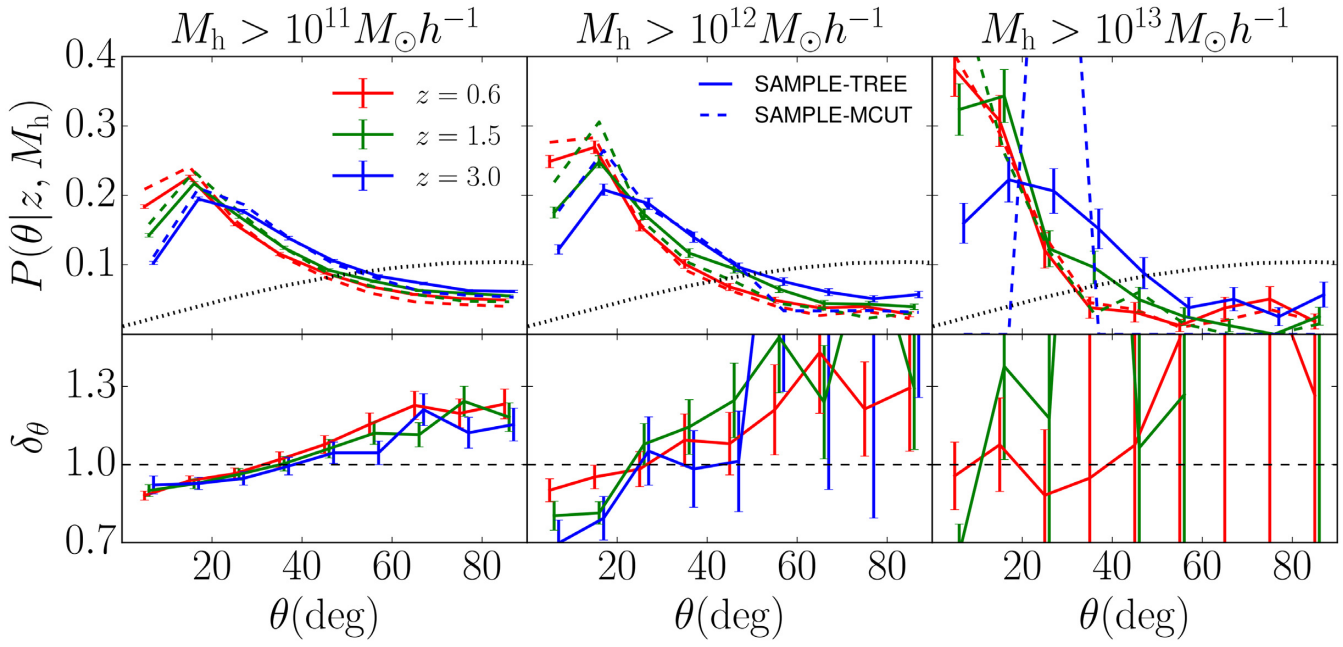

Figure 8. $P(\theta|z, M_h)$ is the distribution of misalignment angle θ between stellar and dark matter component of subhaloes. Solid and dashed lines correspond to SAMPLE-TREE and SAMPLE-MCUT galaxies, respectively. The black dotted lines represent the misalignment angle distribution if the two eigenvectors are uniformly distributed in 3D space. δ_θ is the ratio between the solid and dashed lines. The error bars are obtained via bootstrap resampling.

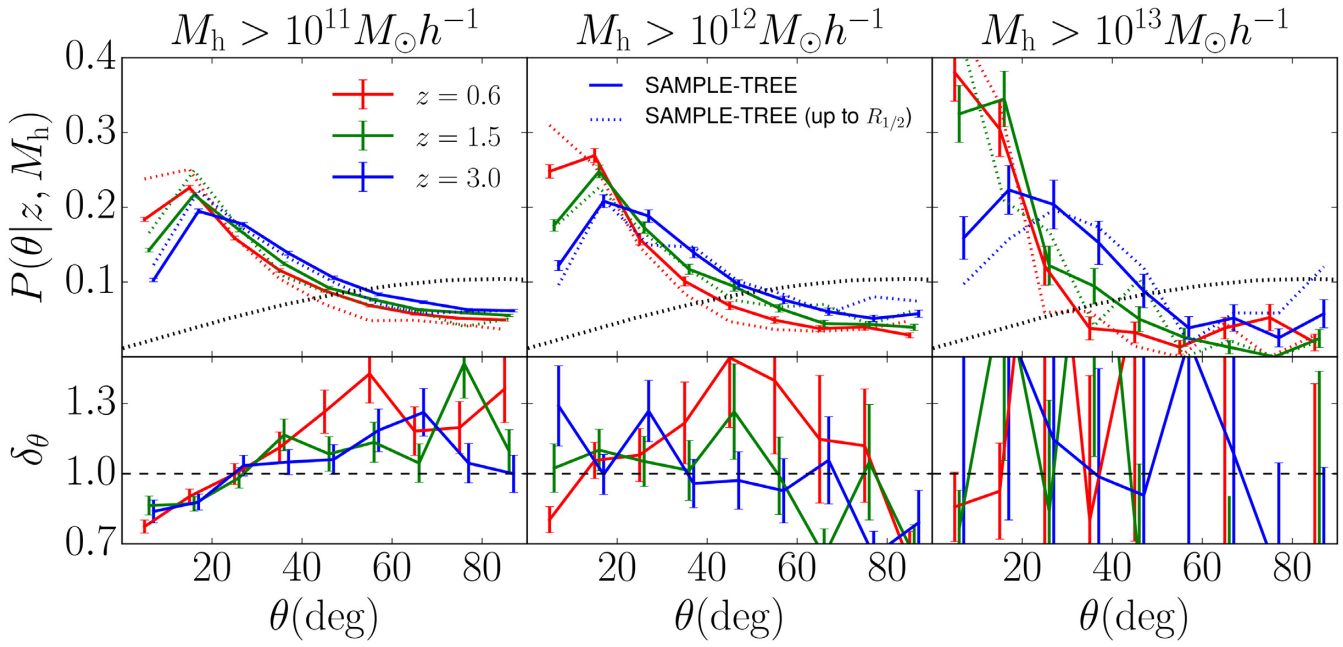

Figure 9. Comparison of the redshift evolution of $P(\theta|z, M_h)$ predictions for SAMPLE-TREE galaxies for different definitions of the inertia tensor. Top panels: the solid lines are obtained using the reduced inertia tensor (same as previous figure). The faded dotted lines correspond to the unweighted inertia tensor for particles within galaxy half-mass radius $R_{1/2}$. The black dotted lines represent the misalignment angle distribution if the two eigenvectors are uniformly distributed in 3D space. δ_θ is the ratio between the solid lines and the dotted lines shown in the top panel. The error bars are obtained via bootstrap resampling.

We have so far discussed the evolution of distributions of galaxy shapes and misalignment angles. In Appendix A, we present the evolution of the average values of the axis ratios and misalignment angles, and provide simple fitting functions to quantify them.

3.4 ED correlation function

In this section, we will investigate how the ED correlation function of galaxies on the merger tree evolves with redshift. We now present the results for the ED correlation function $\omega(r)$. The top panels in Fig. 11 show $\omega(r)$ for SAMPLE-TREE galaxies and its

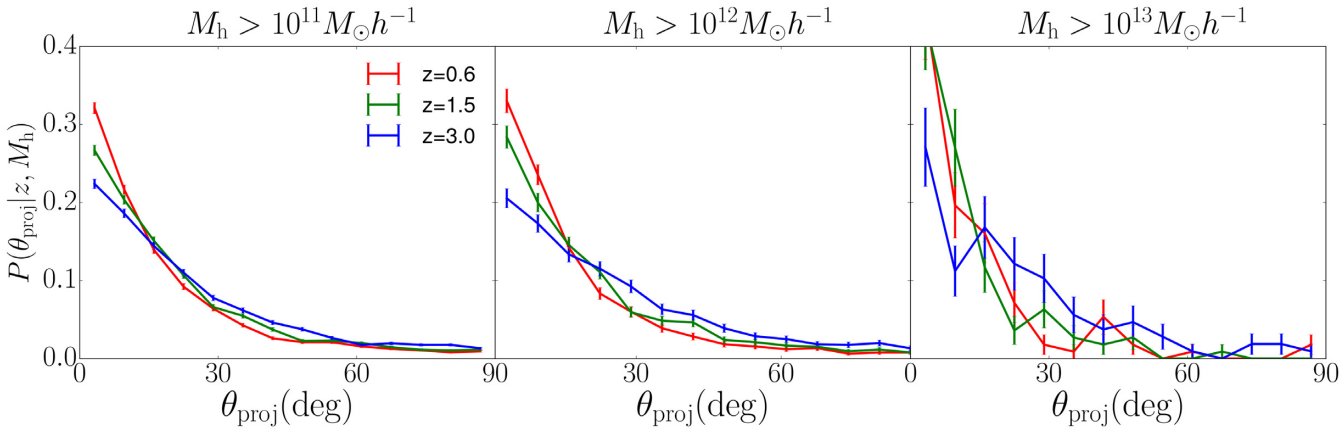

Figure 10. Distribution of projected misalignment angle: $P(\theta_{\rm proj}|z, M_h)$ shows the normalized probability distribution of misalignment angle between the projected stellar and dark matter distributions of the SAMPLE-TREE galaxies on the *xy* plane. The error bars are 1σ Poisson errors.

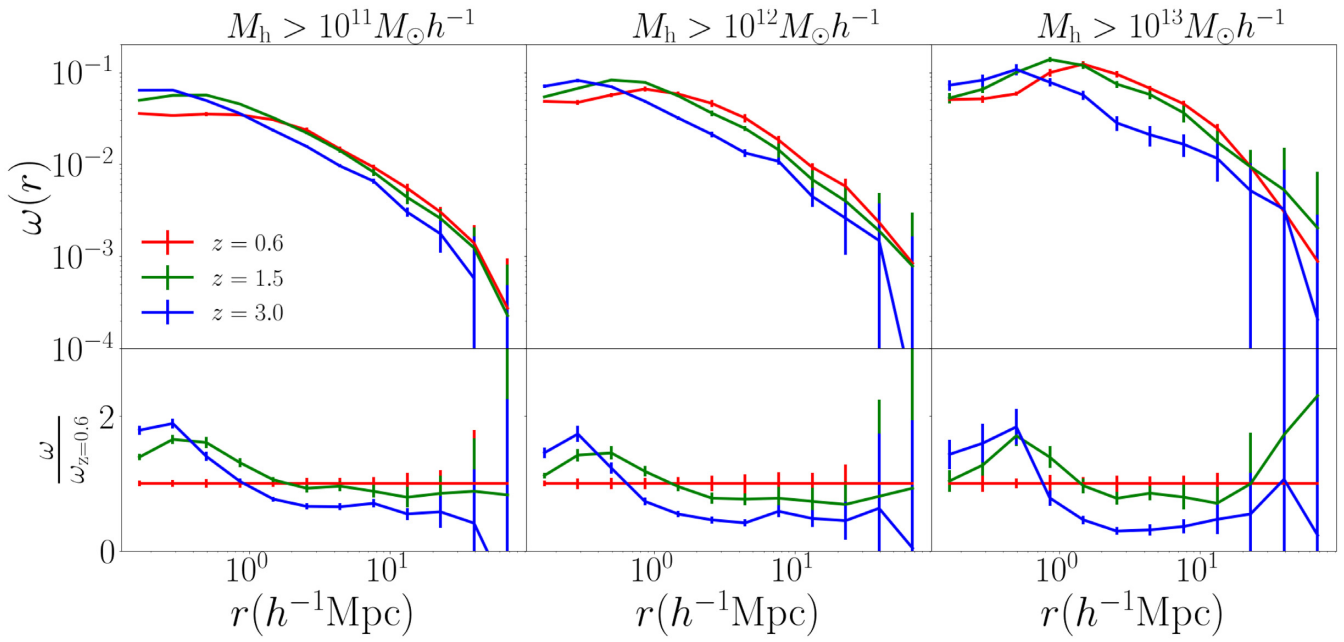

Figure 11. $\omega(r)$ is the ED correlation function of SAMPLE-TREE galaxies at different redshifts. Here, we are using the major axes of the stellar matter components and galaxy positions as tracers of the matter distribution. The bottom panels show the ratio of $\omega(r, z)$ with respect to that of $\omega(r, z = 0.6)$. Error bars are jackknife errors obtained by dividing the simulation volume into eight octants.

redshift evolution along the merger tree. The bottom panels show the ratio $\omega(r, z)/\omega(r, z = 0.6)$. They reveal the evolution of the ED correlation for a wide range of scales to be probed by LSST weak lensing (The LSST Dark Energy Science Collaboration et al. 2018). These include scales $\gtrsim 5$ Mpc h^{-1} where the NLA model and its extensions such as Blazek, Seljak & Mandelbaum (2016) already work well. Additionally, our simulations also reveal ED correlations at smaller scales, which are not well probed by these analytical models. Accordingly, we choose ~ 1 Mpc h^{-1} as an interesting scale around which we shall now describe the evolution of the ED correlation.

At $r > 1$ Mpc h^{-1}, we see that the correlation function is a power law as a function of r. The slope of the power law does not vary significantly with redshift or subhalo mass. The power-law amplitude increases with subhalo mass at fixed redshift, as also reported in Tenneti et al. (2015a). The ED correlation amplitude increases with decreasing redshift along the merger tree (up to factors of $\sim$4 from $z = 3$ to $z = 0.6$).

At sufficiently small scales ($r \lesssim 1$ Mpc h^{-1}), $\omega(r)$ deviates from a power law and is suppressed (compared to power-law extrapolation from large scales). The extent of the suppression increases with decreasing redshift. As we approach even smaller scales ~ 0.1 Mpc h^{-1}, the redshift evolution is reversed compared to large scales, i.e. $\omega(r)$ decreases with decreasing redshift along the merger tree (up to factors of $\sim$2 from $z = 3$ to $z = 0.6$).

We compare $\omega(r)$ predictions of SAMPLE-TREE to that of SAMPLE-MCUT; Fig. 12 shows the ratio between the two as a function of r. We find that as redshift increases, $\omega(r)$ for SAMPLE-TREE becomes increasingly suppressed at scales $r \gtrsim 1$ Mpc h^{-1} as compared to that of SAMPLE-MCUT; at $z = 3$ the suppression is by factors 3–4. At $r \lesssim 1$ Mpc h^{-1}, the differences are relatively small (by factors $\lesssim$2). These differences are largely because SAMPLE-TREE galaxies are less massive compared to SAMPLE-MCUT galaxies at higher redshifts.

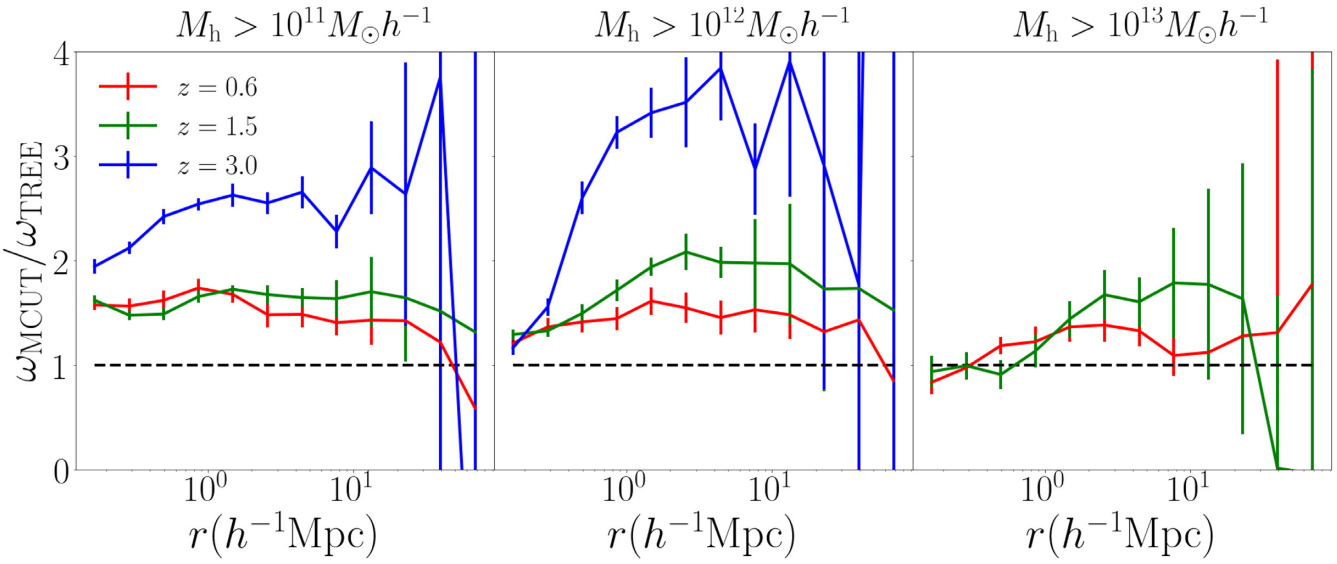

Figure 12. $\omega_{\rm MCUT}/\omega_{\rm TREE}$ is the ratio of $\omega(r)$ of SAMPLE-TREE to that of SAMPLE-MCUT galaxies. Error bars are jackknife errors obtained by dividing the simulation volume into eight octants.

In the following subsections, we shall dig deeper into the foregoing results by first putting them in the context of the galaxy–subhalo misalignments, and then finally revealing the factors that drive the evolution of ED correlations at different scales.

3.4.1 Implications of galaxy–subhalo misalignment on the ED correlation

We now study the implications of galaxy–subhalo misalignment and its evolution on the ED correlation function. To do this, we compare the ED correlations of galaxies (also shown in Fig. 11) to their underlying dark matter subhaloes. The top panel of Fig. 13 shows the ED correlation functions of SAMPLE-TREE galaxies, where the solid and dashed lines correspond to galaxies and dark matter subhaloes, respectively. As a consequence of the misalignment between stellar matter and dark matter, the solid lines showing the galaxy ED correlation functions are significantly suppressed compared to the subhalo ED correlation functions (by factors ∼2–4) at all scales. This implies that the alignment of galaxies with respect to the surrounding density field is suppressed as compared to their dark matter subhaloes. This has been established in previous works (Tenneti et al. 2015b), and is also supported observationally in the alignments of luminous red galaxies (Okumura, Jing & Li 2009). We now discuss how this suppression evolves with redshift on the merger tree. In the bottom panel of Fig. 13, we see that the ratio $\omega_{\rm DMsubhalo}/\omega_{\rm galaxy}$ decreases with decreasing redshift; this is because galaxy–subhalo misalignment decreases with decreasing redshift. Furthermore, the evolution is stronger for $M_h > 10^{11}\,{\rm M}_\odot\,h^{-1}$ haloes as compared to $M_h > 10^{13}\,{\rm M}_\odot\,h^{-1}$. This is because at $z = 3$, $M_h > 10^{13}\,{\rm M}_\odot\,h^{-1}$ galaxies are more aligned with their subhaloes as compared to $M_h > 10^{11}\,{\rm M}_\odot\,h^{-1}$ galaxies (compare leftmost and rightmost panels of Fig. 8).

3.4.2 What drives the evolution of ED correlation at different scales?

Here, we discuss the factors driving the evolution of the galaxy ED correlation at different scales, as inferred from Fig. 13. At scales $\gtrsim 1$ Mpc h^{-1}, note that the ED correlations for dark matter subhaloes (dashed lines) undergo a significantly weaker redshift evolution compared to that of galaxies (solid lines). In fact, there is no significant evolution for $M_h > 10^{11}\,{\rm M}_\odot\,h^{-1}$ and $M_h > 10^{12}\,{\rm M}_\odot\,h^{-1}$ subhaloes. Therefore, the fact that we find a significant evolution for the galaxy ED correlation implies that its evolution at scales > 1 Mpc h^{-1} is primarily driven by the evolution of the galaxy–subhalo misalignment, as opposed to being driven by the ED correlation for dark matter haloes.

At scales $\lesssim 1$ Mpc h^{-1}, a suppression (compared to a power law) is seen in the ED correlations for both galaxies and their dark matter subhaloes. Furthermore, the suppression in the galaxy ED correlation simply traces that of the dark matter subhalo, but at a lower normalization. Overall, this tells us that the evolution of the ED correlation profile for galaxies at scales $\lesssim 1$ Mpc h^{-1} is governed by the evolution of both (i) the ED correlation for dark matter haloes and (ii) the misalignment between galaxies and subhaloes. The former leads to a decrease in the ED correlation for galaxies with time, whereas the latter drives an increase in the ED correlation for galaxies. Due to the complex interplay between these two competing effects, no straightforward trend is seen in the evolution of ED correlation at scales ~ 1 Mpc h^{-1} (to be targeted by LSST).

At very small scales (~ 0.1 Mpc h^{-1}), the suppressed ED correlation of DM subhaloes is so large that it dominates compared to the evolution of galaxy subhalo misalignment angle. This competition causes the reversal in the redshift evolution of $\omega(r)$ for galaxies at these scales, compared to that in scales > 1 Mpc h^{-1}.

4 CONCLUSIONS

This work is part of a continued series of papers dedicated to studying the IAs of galaxies using the MassiveBlackII cosmological hydrodynamic simulation. In this work, we study redshift evolution ($0.6 \lesssim z \lesssim 3$) by selecting galaxy samples (SAMPLE-TREE) based on subhalo mass cuts ($M_h > 10^{11,12,13}\,{\rm M}_\odot\,h^{-1}$) at $z = 0.6$ and tracing their progenitors to $z = 3$ along a merger tree. We study the redshift evolution of galaxy shapes, misalignment with respect to host subhalo, and the ED correlation functions along the merger tree. Our key findings are as follows:

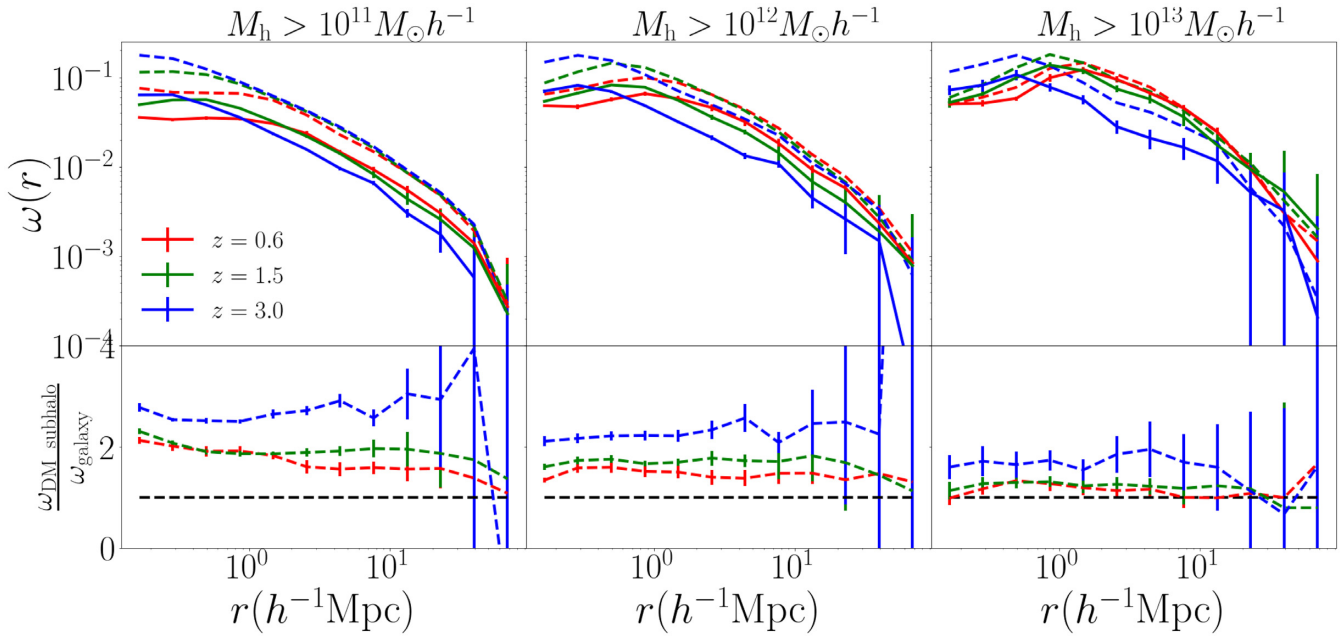

Figure 13. Comparing ED correlation functions for SAMPLE-TREE galaxies and their dark matter subhaloes: in the top panels, solid and dashed lines show the ED correlation functions of galaxies and their dark matter subhaloes, respectively. The ratio between the dashed versus solid lines are shown in the bottom panels. Error bars in the correlation function are jackknife errors obtained by dividing the simulation volume into eight octants.

(i) The sphericity of the dark matter component of galaxies increases with time, whereas that of the stellar matter component decreases with time.

(ii) The distribution of galaxy–subhalo misalignment angle peaks at ∼10 deg. With decreasing redshift, the distribution becomes narrower and more skewed towards smaller misalignment angles.

(iii) The evolution of the ED correlation $\omega(r)$ of galaxies is driven by the evolution of their alignment with respect to their host DM subhaloes, as well as the alignment between DM subhaloes and the surrounding matter overdensity.

(a) At scales ~ 1 Mpc h^{-1}, the alignment between DM subhaloes and the matter overdensity gets suppressed with time. On the other hand, the alignment between galaxies and DM subhaloes is enhanced. Due to these competing tendencies, the redshift evolution of $\omega(r)$ for galaxies at ~ 1 Mpc h^{-1} is not straightforward.

(b) At scales > 1 Mpc h^{-1}, there is no significant evolution in the alignment between DM subhaloes and the matter overdensity. As a result, the evolution of the galaxy–subhalo misalignment leads to an increase in $\omega(r)$ for galaxies by a factor of ∼4 from $z = 3$ to 0.6.

(c) At ~ 0.1 Mpc h^{-1} scales, evolution in $\omega(r)$ for galaxies is completely reversed compared to that at scales $\gtrsim 1$ Mpc h^{-1}, i.e. it decreases by factors ∼2 from $z = 3$ to 0.6. This is because at these scales, the alignment between DM subhaloes and the matter overdensity is strongly suppressed with time, and this effect dominates over evolution of galaxy–subhalo misalignment.

We also compare our results with the sample selection applied in the previous work of this series (Tenneti et al. 2015a). In particular, we also considered galaxy samples (SAMPLE-MCUT) with fixed subhalo mass cuts ($M_h > 10^{11,12,13}$ M$_\odot$ h^{-1}), applied at all redshifts between 0.6 and 3.

Interestingly, upon comparing the sphericities of dark matter components of SAMPLE-TREE and SAMPLE-MCUT galaxies, we find that they do not significantly differ ($\lesssim 10$ per cent); this is true even at the highest redshift ($z = 3$) where SAMPLE-TREE galaxies are significantly less massive than SAMPLE-MCUT. This is explained by our finding that at $z \gtrsim 1.5$, progenitors of $z \sim 0.6$: $M_h \gtrsim 10^{11}$ M$_\odot$ h^{-1} galaxies have significantly less spherical (on an average) dark matter shapes than a *randomly selected* galaxy of similar subhalo mass and redshift.

For the stellar matter component, we find that SAMPLE-TREE progenitors at $z = 3$ are less spherical compared to SAMPLE-MCUT galaxies. This is because SAMPLE-MCUT galaxies are more massive (which we show to be more spherical for stellar matter component) than SAMPLE-TREE galaxies at $z = 3$.

We find that SAMPLE-TREE galaxies are less aligned with their subhaloes compared to SAMPLE-MCUT galaxies. At $z = 1.5$ and $z = 3$, this can be attributed to the differences between their subhalo masses. But the fact that we also see this at $z = 0.6$ further implies that galaxies that formed earlier than $z = 3$ (i.e. those that do not have progenitors up to $z = 3$) are more aligned than those that formed at $z < 3$.

The effect of differences in subhalo masses (at $z > 0.6$) of SAMPLE-TREE and SAMPLE-MCUT galaxies is also seen in their ED correlation function $\omega(r)$. Compared to SAMPLE-MCUT, $\omega(r)$ for SAMPLE-TREE galaxies is suppressed at increasing redshift (by factors up to ∼3–4 at $z = 3$); this is due to decreasing subhalo masses of progenitors in SAMPLE-TREE at increasing redshift.

This work demonstrates that hydrodynamic simulations such as MBII are dispensable tools to study redshift evolution of galaxy properties such as IA, primarily because of the ability to directly trace progenitors of present-day galaxies by constructing merger trees. This enables us to disentangle true IA evolution from apparent evolution due to sample selection effects, which are inevitable in observations. Future work will involve the use of the results from this study, as well as previous works (Tenneti et al. 2014, 2015a, 2016), to construct halo models for IA of galaxies. These models can then be used to construct mock catalogues by populating *N*-

body simulation volumes, and thereby analyse possible systematic biases caused by IA in weak lensing analyses.

ACKNOWLEDGEMENTS

We thank Yu Feng for providing the data of MBII simulation snapshots and raw data. This research is supported by the US National Science Foundation under Grant No. 1716131. TDM acknowledges funding from NSF ACI-1614853, NSF AST-1517593, NSF AST-1616168, NASA ATP 80NSSC18K1015, and NASA ATP 17-0123.

REFERENCES

Abell P. A. et al., 2009, preprint (arXiv:0912.0201)
Allgood B., Flores R. A., Primack J. R., Kravtsov A. V., Wechsler R. H., Faltenbacher A., Bullock J. S., 2006, MNRAS, 367, 1781
Bailin J., Steinmetz M., 2005, ApJ, 627, 647
Behroozi P. S., Wechsler R. H., Wu H.-Y., 2012a, ApJ, 762, 109
Behroozi P. S., Wechsler R. H., Wu H.-Y., Busha M. T., Klypin A. A., Primack J. R., 2012b, ApJ, 763, 18
Behroozi P. S., Wechsler R. H., Conroy C., 2013, ApJ, 770, 57
Blazek J., Vlah Z., Seljak U., 2015, J. Cosmol. Astropart. Phys., 2015, 015
Blazek J., Seljak U., Mandelbaum R., 2016, in van de Weygaert R., Shandarin S., Saar E., Einasto J., eds, IAU Symp. Vol. 308, The Zeldovich Universe: Genesis and Growth of the Cosmic Web. Cambridge Univ. Press, Cambridge, p. 452
Bridle S., King L., 2007, New J. Phys., 9, 444
Camelio G., Lombardi M., 2015, A&A, 575, A113
Catelan P., Kamionkowski M., Blandford R. D., 2001, MNRAS, 320, L7
Chisari N. et al., 2015, MNRAS, 454, 2736
Chisari N. E. et al., 2017, MNRAS, 472, 1163
Davis M., Efstathiou G., Frenk C. S., White S. D., 1985, ApJ, 292, 371
Dubois Y. et al., 2014, MNRAS, 444, 1453
Hilbert S., Xu D., Schneider P., Springel V., Vogelsberger M., Hernquist L., 2017, MNRAS, 468, 790
Hirata C. M., Seljak U., 2004, Phys. Rev. D, 70, 063526
Hirata C. M., Mandelbaum R., Ishak M., Seljak U., Nichol R., Pimbblet K. A., Ross N. P., Wake D., 2007, MNRAS, 381, 1197
Hopkins P. F., Bahcall N. A., Bode P., 2005, ApJ, 618, 1
Ivezić Ž. et al., 2008, ApJ, 873, 111
Joachimi B., Mandelbaum R., Abdalla F. B., Bridle S. L., 2011, A&A, 527, A26
Joachimi B. et al., 2015, Space Sci. Rev., 193, 1
Khandai N., Di Matteo T., Croft R., Wilkins S., Feng Y., Tucker E., DeGraf C., Liu M.-S., 2015, MNRAS, 450, 1349
Kiessling A. et al., 2015, Space Sci. Rev., 193, 67
Kirk D. et al., 2015, Space Sci. Rev., 193, 139
Komatsu E.(Collaboration WMAP), et al., (Collaboration WMAP), 2011, Astrophys. J. Suppl, 192, 645
Krause E., Eifler T., Blazek J., 2016, MNRAS, 456, 207
Laureijs R. et al., 2011, preprint (arXiv:1110.3193)
Leauthaud A. et al., 2012, ApJ, 744, 159
Lee J., Springel V., Pen U.-L., Lemson G., 2008, MNRAS, 389, 1266
Mandelbaum R., 2018, ARA&A, 56, 393
Mandelbaum R., Hirata C. M., Ishak M., Seljak U., Brinkmann J., 2006, MNRAS, 367, 611
Mitchell P. D., Lacey C. G., Baugh C. M., Cole S., 2016, MNRAS, 456, 1459
Okumura T., Jing Y. P., Li C., 2009, ApJ, 694, 214
Schaye J. et al., 2015, MNRAS, 446, 521
Singh S., Mandelbaum R., More S., 2015, MNRAS, 450, 2195
Spergel D. et al., 2015, preprint (arXiv:1503.03757)
Springel V., White S. D., Tormen G., Kauffmann G., 2001, MNRAS, 328, 726
Tenneti A., Mandelbaum R., Di Matteo T., Feng Y., Khandai N., 2014, MNRAS, 441, 470
Tenneti A., Singh S., Mandelbaum R., Matteo T. D., Feng Y., Khandai N., 2015a, MNRAS, 448, 3522
Tenneti A., Mandelbaum R., Di Matteo T., Kiessling A., Khandai N., 2015b, MNRAS, 453, 469
Tenneti A., Mandelbaum R., Di Matteo T., 2016, MNRAS, 462, 2668
The LSST Dark Energy Science Collaboration et al., 2018, preprint (arXiv:1809.01669)
Troxel M., Ishak M., 2015, Phys. Rep., 558, 1
Velliscig M. et al., 2015, MNRAS, 454, 3328
Vogelsberger M. et al., 2014, MNRAS, 444, 1518

APPENDIX A: FITTING THE EVOLUTION OF SHAPE AND MISALIGNMENT ANGLE

Here, we present fitting functions for the evolution of the axis ratios and misalignment angles. We model the redshift evolution as a

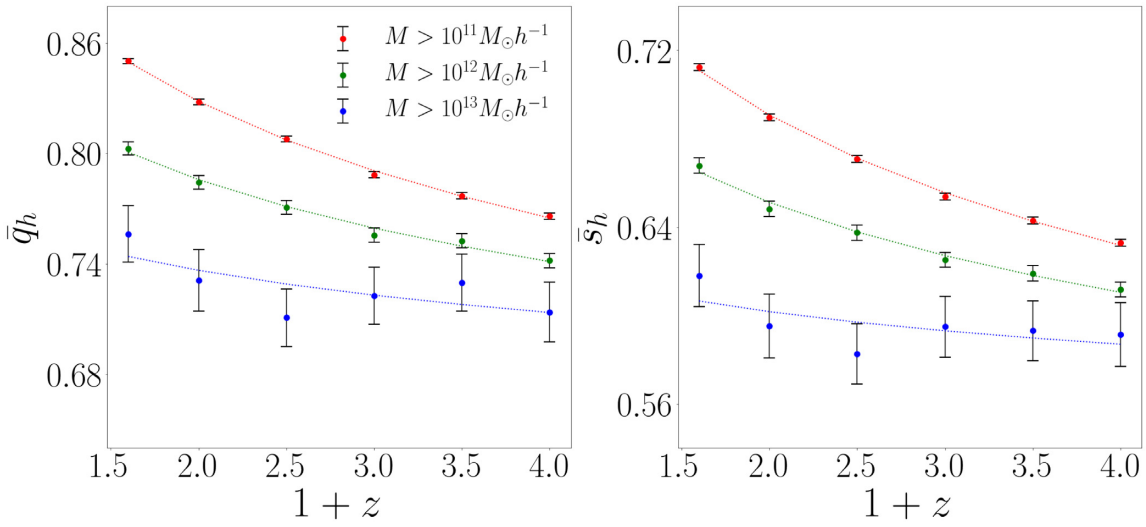

Figure A1. The filled circles show $q_h^{\max}$ and $s_h^{\max}$, which correspond to the averages of the distributions $P(q|M_h, z)$ and $P(s|M_h, z)$ for the dark matter component of SAMPLE-TREE galaxies. The dashed lines show the best-fitting trend described by the function in equation (A1). The error bars are jackknife errors obtained by dividing the simulation volume into eight octants.

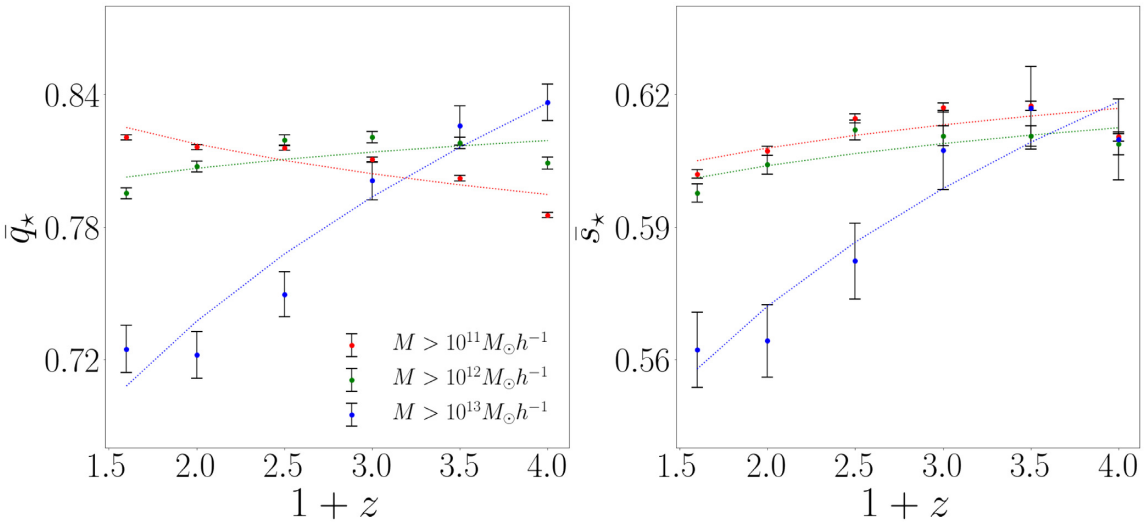

Figure A2. The filled circles show $q_*^{\max}$ and $s_*^{\max}$, which correspond to the averages of the distributions $P(q|M_h, z)$ and $P(s|M_h, z)$ for the stellar matter component of SAMPLE-TREE galaxies. The dashed lines show the best-fitting trend described by the function in equation (A1). The error bars are jackknife errors obtained by dividing the simulation volume into eight octants.

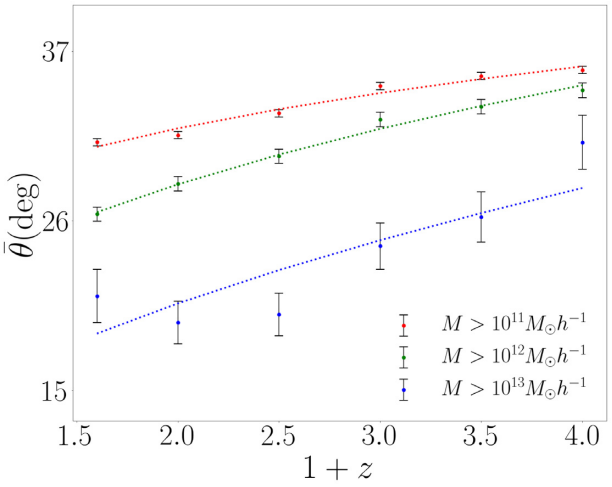

Figure A3. The filled circles show $\theta^{\max}$, which corresponds to the peaks of the distributions $P(\theta|M_h, z)$ for the dark matter component of SAMPLE-TREE galaxies. The dashed lines show the best-fitting trend described by the function in equation (A1).

Table A1. Best-fitting values of X_0 and α_X for various quantities: q_h and s_h are q and s values of dark matter and stellar matter component of the SAMPLE-TREE galaxies (subhaloes), respectively.

X	X_0	α_X
q_h	0.897	0.115
s_h	0.756	0.129
$q_\star$	0.841	0.04
$s_\star$	0.599	− 0.02
θ	28.4	− 0.170

power law

$$\bar{X} = X_0(1+z)^{-\alpha_X} \tag{A1}$$

where X represent the quantity of interest (axis ratios/misalignment angle). $\bar{X}$ is the average value of the distribution $P(X|M_H, z)$. X_0 is the value of $\bar{X}$ at $z = 0$. The filled circles in Figs A1, A2, and A3 correspond to the average of the distributions of axis ratios and misalignment angles. The dashed lines show the best fits obtained using equation (A1). The corresponding best-fitting parameters are shown in Table A1.

APPENDIX B: COMPUTING THE STELLAR SHAPE PARAMETERS WITHIN THE HALF-MASS RADII OF GALAXIES

In Section 3.3.1, we computed (in addition to stellar shapes with *reduced* inertia tensor) the stellar shapes effectively within the half-mass radii of galaxies using *unweighted* (iterative) inertia tensor. However, as mentioned in Section 3.3.1, simply excluding all stars outside a sphere of half-mass radius artificially imposes a spherical symmetry in the stellar distributions; this can potentially bias the inferred shapes towards being more spherical. In order to avoid this bias, we instead consider ellipsoids and perform the iterative scheme in the following manner. At the first iteration, we include all the stars within the subhalo, and determine the eigenvectors $(\hat{e}_a, \hat{e}_b, \hat{e}_c)$ and (a, b, c). At the second iteration and thereafter, we consider an ellipsoid with principal axes and axis ratios obtained from the previous iteration, but scale down the volume such that it is equal to that of a sphere with half-mass radius. In particular, for iteration i with eigenvectors $(\hat{e}_a^i, \hat{e}_b^i, \hat{e}_c^i)$, eigenvalues (a^i, b^i, c^i), and axis ratios (q^i, s^i), we have for $i \geq 2$

$$\left(\hat{e}_a^i, \hat{e}_b^i, \hat{e}_c^i\right) = \left(\hat{e}_a^{i-1}, \hat{e}_b^{i-1}, \hat{e}_c^{i-1}\right) \tag{B1}$$

$$(q^i, s^i) = (q^{i-1}, s^{i-1}) \tag{B2}$$

$$(a_i, b_i, c_i) = (a_{i-1}R_{i-1}, b_{i-1}R_{i-1}, c_{i-1}R_{i-1}); \tag{B3}$$

where $R_i = \frac{r_{1/2}}{(a_i b_i c_i)^{1/3}}$. The end of the iteration is marked by when the shape parameters converge, which then corresponds to an unbiased measurement of the galaxy shape.

This paper has been typeset from a TEX/LATEX file prepared by the author.